Improving the Reliability/Cost Ratio of Goniophotometric Comparisons

Aravind Krishnaswamy   Gladimir V. G. Baranoski   Jon G. Rokne
University of Waterloo   University of Waterloo   University of Calgary

Abstract. Many scattering models have been presented in the graphics literature. Few of them, however, have been evaluated through comparisons with real measured data. As the demand for plausible and predictable scattering models increases, more attention is given to performing such comparisons. In this paper we examine the implementation of virtual goniphotometers used to obtain BRDF (bidirectional reflectance distribution function) and BTDF (bidirectional transmittance distribution function) records from algorithmic scattering models. These records can be compared to data from actual experiments in order to validate the models. Our discussion focuses on practical issues, namely the subdivision of the devices' collector sphere and the ray density required to obtain reliable BRDF and BTDF estimates. The subdivision techniques examined in this paper have been used before in publications, but the details of their computation are not readily available in the literature. Although the mathematical bound presented to determine appropriate ray densities for virtual goniphotometers is a direct generalization of a bound used for virtual spectrophotometers, it has not been published before. Our discussion of these issues is supported by practical experiments whose results are also provided in this paper.

1 Introduction

Greenberg *et al.* [15] proposed a framework to test, validate and improve the fidelity and efficiency of computer graphics algorithms composed of three stages, namely local light scattering models, light transport simulations and image display procedures. They emphasized the importance of performing comparisons between simulations and actual measurements so that simulations can be used in a predictive manner. According to their paradigm, it is of fundamental importance that simulations are compared with measured experiments at each stage.

In this paper we focus on issues related to the first stage of this system, more specifically the evaluation of algorithmic scattering models. These evaluations involve comparisons of readings provided by a model with actual BRDF measurements performed using goniophotometers [17, 19]. In order to obtain these readings from a computer model in the first place, one must perform a computer simulation of the inputs and outputs of the model, *i.e.*, use virtual goniophotometers. These devices also have important applications not only in graphics [27, 6, 11, 22], but also in areas such as remote sensing [14] and medicine [30]. The formulation of such devices has to reproduce actual measurement conditions as faithfully as possible to avoid the introduction of bias in the comparisons.

These virtual devices are used not only to determine the plausibility of scattering models, but also to perform data collection from previously validated models. Besides giving users a control over the spectral data generation from computer models used to simulate the scattering profile of various materials, these devices also allow users to perform experiments at different sampling resolutions [22], which are important requirements in rendering.

When such virtual devices are found in the computer graphics literature, it is usually in connection with a scattering model. For example, Gondek *et al.* [12] have used a virtual goniospectrophotometer for spectral and spatial measurements presented as an optics model and a capture dome used in conjunction with a geometric model of surface microstructure. Although our discussion is related to applications involving algorithmic scattering models, the main goal is to address the formulation of virtual goniophotometers, and closely examine implementation and usage issues (collector sphere subdivision and ray density) that affect the reliability/cost ratio of the measurements, without focusing on any specific scattering model.

2 Background Information

2.1 General Characteristics of Actual Goniophotometers

A goniophotometer (from greek: gonio-photo-meter=angle-light-measuring) is defined as an instrument that measures radiant flux (power) as a function of angles of illumination and observation [7]. These measurements can be performed in different ways, and, as a result, there are many possible configurations for these devices. Computer graphics researchers have proposed extensions for industrially made goniophotometers [9] as well as new designs based on the use of digital cameras [20, 31, 24]. A review of these devices is beyond the scope of this work. A reader interested in more detailed description of goniophotometers used in computer graphics is referred to more comprehensive works in this area [9, 25].

Goniophotometers are also important basic tools for fundamental research in colorimetry [23], solar engineering [8], plant biochemistry [2, 18] and remote sensing [5, 18]. For instance, Figure 1 (left) shows a photograph of a goniophotometer used by Combes *et al.* [4] to measure BRDFs of plant specimens. The light flux which is incident on the specimen comes from an emitter. After being reflected or transmitted by the specimen, it is captured by a detector (photometer).

A comprehensive goniophotometric record for a simple specimen requires a formidable number of measurements as mentioned by Judd and Wyszecki [19] and Greenberg *et al.* [15]. Both the emitter and the photometer have to be moved independently of one another to every position on the hemisphere. In order to illustrate this aspect Judd and Wyszecki performed the following calculation. They assumed a fairly large solid angle of approximately 0.005 steradian for each aperture. To cover the entire hemisphere (2π steradian) as closely as possible with such an aperture without overlapping, they had to use about 1000 different positions. With both the source and the photometer moved in each of the 1000 positions, 1 million measurements would be required!

The best-designed, best-constructed and best-calibrated spectrophotometers may also yield results that differ from one measurement to the next. These differences, or uncertainties, are net results of combinations of many small fluctuations due to independent variations of different components of the instrument, different factors in the environment and how the specimen is handled.
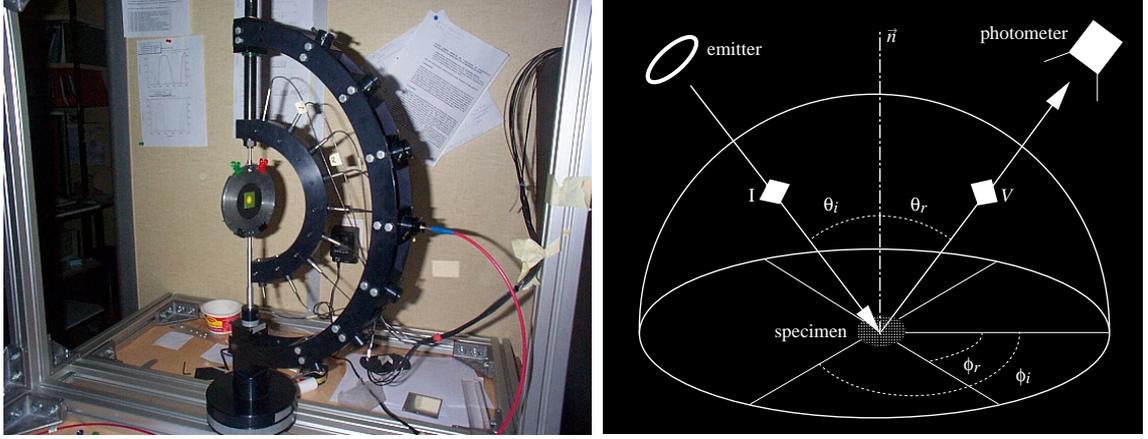
Figure 1: Left: photograph of a goniophotometer (courtesy of Stephane Jacquemoud). Right: sketch of a virtual goniophotometer.

2.2 General Formulation of Virtual Goniophotometers

In order to simulate radiance measurements performed by placing a photometer at different viewing positions, one can use radiance detectors, which are represented by the patches of a collector sphere placed around a specimen. Figure 1 (right) presents a sketch showing the principal components of a virtual goniophotometer and their geometrical arrangement. The light flux incident on the specimen comes from the emitter through patch I, and the light flux collected by the photometer comes through patch V. Both of the illuminating and viewing directions can be varied independently within the hemisphere above the specimen. The position of emitter and patch I is given by the azimuth angle ϕ_i and the polar angle θ_i. The position of photometer and patch V is given by the azimuth angle ϕ_r and the polar angle θ_r.

Using this arrangement, the BRDF for a direction associated with a given radiance detector placed in the upper hemisphere can be determined in terms of radiant power. More specifically, it is given by the ratio between the radiant power reaching the detector, Φ^r, after interacting with the specimen, and the incident radiant power, Φ^i [13].

The corresponding expression used to compute the BRDF for light incident at wavelength λ, considering the solid angle in the direction of incidence, $\vec{\omega_i}$, and the solid angle in the direction associated with the radiance detector, $\vec{\omega_r}$, is given by:

$$f_r(\lambda, \vec{\omega_i}, \vec{\omega_r}) = \frac{\Phi^r(\lambda)}{\Phi^i(\lambda)\ \vec{\omega_r}^p} \tag{1}$$

where:
$\vec{\omega_r}^p$ = adjusted solid angle regarding the direction associated with the radiance detector.

In turn, the adjusted solid angle $\vec{\omega_r}^p$ is given by:

$$\vec{\omega_r}^p = \frac{A_r \cos\theta_r}{L^2} \tag{2}$$

where:
A_r = area of the radiance detector (represented by patch V in Figure 1),
L = distance from the specimen to the radiance detector, *i.e.*, the radius of the hemisphere shown in Figure 1,
θ_r = angle between the direction associated with the radiance detector and the specimen normal.

Consider N rays shot towards the specimen for a given wavelength λ, and assume that each ray carries the same amount of radiant power, Φ. If the total radiant power to be shot is Φ_i, then the radiant power carried by each ray is given by [28]:

$$\Phi_{ray}(\lambda) = \frac{\Phi_i(\lambda)}{N} \tag{3}$$

Also, the radiant power reaching the radiance detector can be written as:

$$\Phi^r(\lambda) = n_r \Phi_{ray}(\lambda) \tag{4}$$

where:
n_r = number of rays hitting a radiance detector.

Thus, replacing Equation 3 and Equation 4 in Equation 1, the expression to compute the BRDF reduces to:

$$f_r(\lambda, \vec{\omega_i}, \vec{\omega_r}) = \frac{n_r}{N\ \vec{\omega_r}^p} \tag{5}$$

Similarly the BTDF is calculated assuming the radiance detectors are placed in the lower hemisphere.

For applications involving data generation from a previously validated model, the sample rays are usually collimated, *i.e.*, the sample rays have the same origin and they hit the specimen at the same point. For applications involving comparisons with actual measurements the sample rays may need to be distributed angularly according to the geometrical arrangement of the surfaces used to represent the emitter and the specimen. As mentioned by Crowther [5], the incident radiation from an emitter shows no preference for one angular region over the other. So, in order to simulate these measurement conditions, the origins and targets of the rays are random points (or sample points) chosen on the surfaces used to represent the emitter and the specimen respectively. Several sampling strategies can be used to select these sample points. In this paper we do not intend to determine the most accurate or the most efficient sampling strategy, since the advantages and drawbacks of different sampling strategies have been adequately covered elsewhere [10, 28, 29].

3 Collector Sphere Subdivision

The first questions that come to mind when one starts the implementation of a virtual goniophotometer are: "How should the collector sphere be subdivided?" and "Does it matter?". In this section we describe three subdivision approaches and address their merits and limitations. We choose these approaches because they do not require prior knowledge about the behavior of the BRDF and their implementation is relatively straightforward. Is important to note, however, that there are alternatives available in the literature, such as the triangular tessellation centered on the specular direction used by Gondek *et al.* [12], in which the patterns used to measure the samples concentrate in areas of greatest change in the BRDF.

3.1 Equal Angular Intervals

The simplest way to subdivide the collector sphere into patches is to use spherical coordinates, $\phi \in [0, 2\pi]$ and $\theta \in [0, \frac{\pi}{2}]$, sampled at equal angular intervals along both coordinate directions. In this case the resulting patches will not have the same area, and it should be noted that the computation of the BRDFs involves the computation of the adjusted solid angle (Equation 2) for each patch, which, in turn involves the computation of the area of the patch and the specification of the angle θ_r.

Consider a patch given by the spherical coordinates (θ_1, θ_2) and (ϕ_1, ϕ_2). One might think that θ_r should correspond to $\frac{\theta_1 + \theta_2}{2}$. But because the computation of the BRDF estimates involves $\cos \theta_r$, we can obtain more accurate results using $\theta_r = \arccos(\frac{\cos(\theta_1) + \cos(\theta_2)}{2})$ when the sphere is subdivided into a small number of patches. As one subdivides the sphere into a larger number of patches, the BRDF estimates computed using the first approach (averaging in terms of θ) and BRDF estimates computed using the second approach (averaging in terms of $\cos \theta$) converge to the same values since the angle θ_r tends to be the same for both approaches. These aspects are illustrated in Figure 2, which shows a graph of numerical experiments performed to compare the $\cos \theta_r$ values obtained using the two approaches for selecting the angle θ_r.
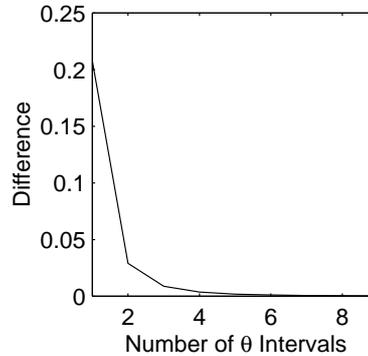
Figure 2: Differences between $\cos \theta_r$ values computed using θ_r averaged in terms of θ and averaged in terms of $\cos \theta$. The differences are given as a function of the number of divisions of the upper hemisphere in the θ direction.

3.2 Equal Solid Angles

Another approach that can be applied is the subdivision of the collector sphere into regions of equal solid angles [16], *i.e.*, the patches on the collector sphere will have the same area. In this case the parameter space represented by $\phi \in [0, 2\pi]$ will be divided into equal intervals as in the previous case. The values for the spherical coordinate θ are chosen to guarantee equal area patches.

Considering the geometry presented in Figure 3, the small triangle has the relationship:

$$\frac{dh}{ds} = \sin d\theta \tag{6}$$

and the large the relationship:

$$\frac{h_1}{L} = \sin \theta \tag{7}$$

and

$$\frac{L'}{L} = \cos\theta \tag{8}$$

so

$$L' = L \cos\theta \tag{9}$$

The integral of the spherical segment between h_1 and h_2 is therefore:

$$\int_{h_1}^{h_2} 2\pi \ L' \ ds = \int_{h_1}^{h_2} 2\pi \ L \ \cos\theta \frac{dh}{\cos\theta} = \int_{h_1}^{h_2} 2\pi \ L \ dh = 2\pi \ L \ (h_2 - h_1) \tag{10}$$

Hence, each slice of the same thickness, $(h_2 - h_1)$, has the same surface area around the slice.
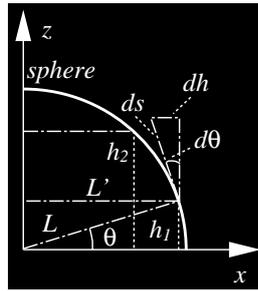
Figure 3: Geometry used to subdivide the collector sphere into equal solid angle regions.

Considering the upper hemisphere divided into m_s equal thickness slices, the angles θ_1 and θ_2 limiting a given patch are given by:

$$(\theta_1, \theta_2) = \left(\arccos(\frac{h_1}{L}), \arccos(\frac{(h_1 + \frac{L}{m_s})}{L}) \right) \tag{11}$$

The issues raised in the previous section with respect to the choice for θ_r also apply to this subdivision approach. In fact our experiments (Section 5.1) show minor improvements in the accuracy of the measurements. The computation of the areas, however, can be done more efficiently than in the previous case, since all patches have the same area. In the equal angular intervals technique the areas are not the same for all patches, which requires more computation.

3.3 Equal Adjusted Solid Angles

The third approach examined in this paper has not been referenced before to the best of our knowledge. It consists of subdividing the collector sphere into regions of equal adjusted solid angles. Like in the previous cases, the parameter space represented by $\phi \in [0, 2\pi]$ is divided into equal intervals. The values for the spherical coordinate θ are computed taking into account the definition of adjusted solid angles given by Equation 1, whose numerator is used in the Nusselt analog [26] to provide a geometric equivalent to the differential area-to-area form factor [3].

Consider a patch on the upper hemisphere above the specimen. Its adjusted solid angle is given by:

$$\int_{\phi=0}^{\phi=2\pi} \int_{\theta=\theta_1}^{\theta=\theta_2} \cos\theta \ \sin\theta \ d\theta \ d\phi = 2\pi \left[\frac{\cos^2 0}{2} - \frac{\cos^2 \frac{\pi}{2}}{2} \right] \tag{12}$$

Using the integration above, the adjusted solid angle of a slice limited by θ_1 and θ_2 is given $\pi[cos^2\theta_1 - cos^2\theta_2]$. To divide the hemisphere into m_s regions in the θ direction the region-bounding values of θ can therefore be computed as:

$$\theta_i = \arccos\sqrt{(1 - \frac{i}{m_s})}, \quad for \quad i = 0, ..., m_s \tag{13}$$

In this approach the choice of θ_r is embedded in the integration leading to the equal adjusted solid angles. As a result, the computation of the adjusted solid angles is performed more accurately. Moreover, our experiments (Section 5.1) show that it enables a more uniform convergence of the BRDF estimates than the previous techniques.

4 Ray Density

Another key question to be addressed when performing virtual goniophotometric measurements is how many rays should be cast by the emitter element, *i.e.*, how large should N be, 10^5, 10^9 or 10^{15}? Using a sufficiently large number of sample rays, one will have a high probability of obtaining estimates within the region of asymptotic convergence of the expected values of a BRDF being measured. The computational costs, however, grow linearly with respect to the total number of sample rays N since the implementation cost is constant per

ray. The purpose of the following derivation is, therefore, to provide a satisfactory bound for N such that we can obtain BRDF estimates with a higher reliability/cost ratio. In this context the term "satisfactory" means taking into account the uncertainty of the actual goniophotometer whose readings we are comparing the measurements with, and aiming at an error tolerance compatible with rendering requirements.

Baranoski *et al.* [1] have shown that the exponential Chebyshev inequality can be applied to obtain a bound for the number of sample rays required to obtain an asymptotically convergent value for the ratio $\frac{n_r}{N}$ with respect to a single radiance detector r. In this case, it can be shown [1] that:

$$P\left\{\left|\frac{n_r}{N} - p_r\right| < \epsilon\right\} \geq 1 - 2e^{-2N\epsilon^2} \tag{14}$$

where:

$P(w)$	$=$	probability of w,
p_r	$=$	probability of a ray hitting the radiance detector r,
ϵ	$=$	error tolerance.

Theoretically, the confidence δ in an estimation is a positive number such that:

$$\delta \geq 1 - P\left\{\left|\frac{n_r}{N} - p_r\right| < \epsilon\right\} \tag{15}$$

where

$$\delta \geq \frac{1}{4N\epsilon^2} \tag{16}$$

Using the inequalities above, Baranoski *et al.* [1] showed that the bound on the number of sample rays is given by:

$$N = \left\lceil \frac{\ln(\frac{2}{\delta})}{2\epsilon^2} \right\rceil \tag{17}$$

The behavior of this bound is illustrated in Figure 4, which shows the number of samples rays required for given values of error tolerance and confidence.
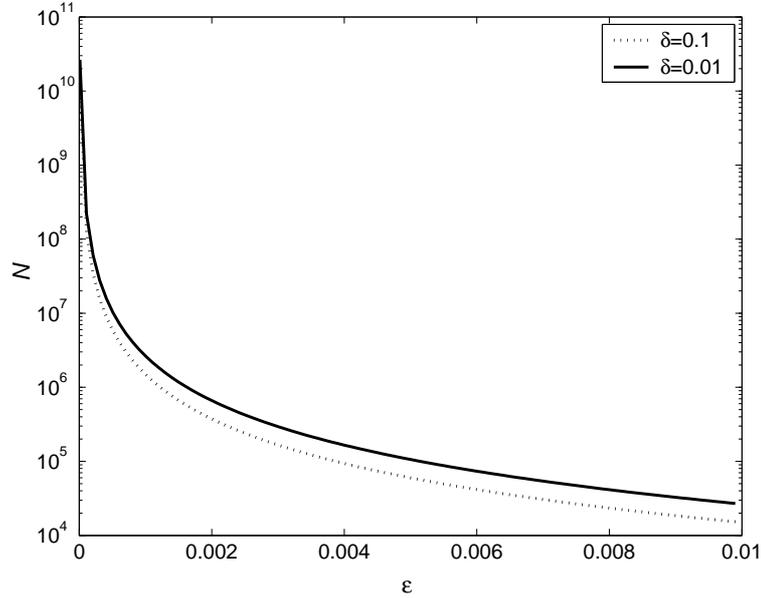
Figure 4: Number of rays (N) required to obtain estimates with a given error tolerance (ϵ), considering different confidence (δ) values.

These inequalities can be generalized for m patches (or radiance detectors) as follows:

$$P\left\{\cap(\left|\frac{n_i}{N} - p_i\right| < \epsilon)\right\} = \prod_{i=1}^{m} P\left\{\left|\frac{n_i}{N} - p_i\right| < \epsilon\right\} \geq \prod_{i=1}^{m}(1 - 2e^{-2N\epsilon^2}) \geq 1 - (\sum_{i=1}^{m} 2e^{-2N\epsilon^2}) = 1 - 2m\,e^{-2N\epsilon^2} \geq 1 - \delta^m \tag{18}$$

Resulting in:

$$\delta \geq \sqrt[m]{2m}\;e^{\frac{-2N\epsilon^2}{m}} \tag{19}$$

For large values of m, the inequality above reduces to:

$$\delta \geq e^{\frac{-2N\epsilon^2}{m}} \tag{20}$$

and the number of rays is given by:

$$N = m \left\lceil \frac{\ln(\frac{2}{\delta})}{2\epsilon^2} \right\rceil \qquad (21)$$

Note that N represents the number of sample rays required to obtain asymptotically convergent values for the ratio $\frac{\Phi^r(\lambda)}{\Phi^i(\lambda)}$, which is then scaled by the adjusted solid angle in order to obtain the corresponding BRDF value (Equation 1).

The value provided by N represents an upper bound assuming the worst case scenario where all patches receive hits (*e.g.*, a Lambertian or diffuse specimen). For models simulating materials with a strong directional behavior, the number of rays required to obtain asymptotically convergent results will be at least one order of magnitude smaller than the number provided by the proposed bound as illustrated in Section 5.2. This aspect suggests that m in the proposed bound could be replace by m' representing the number of patches on the collector sphere within the directional lobe. This parameter, however, is usually unknown *a priori*. If we had an estimate for it, we could also use this estimate to guide a non-uniform distribution of the collector patches as suggested by Greenberg *et al.* [15]. In the extreme case of a mirror-like BRDF, m' is equal to one. Applying the bound given in Equation 21, $N = 10^{5.05}$ rays would be sufficient to obtain asymptotically convergent results, which corresponds to the number of rays required to obtain an asymptotically convergent value for the ratio $\frac{n_r}{N}$ with respect to a single radiance detector (patch).

5   Experiments and Discussion

The experiments presented in this section address implementation and usage issues directly associated with the reliability of virtual goniophotometers in general, *i.e.*, we are not targeting the reproduction of measurements performed by a specific goniophotometer. Hence, we use a virtual device whose collector sphere has unit radius and consider collimated incident beams in these experiments. For the sake of consistency we use the same angle of incidence ($45°$) in all experiments. Since the procedures are the same for both BRDF and BTDF measurements, we focus our observations on the former and work with the upper hemisphere.

5.1   Subdivision Errors

In our evaluation of error propagation associated with the subdivision techniques described in Section 3, we consider a specimen with perfect diffuse (Lambertian) reflective properties for two reasons. First, its BRDF with respect to any direction is known, *i.e.*, $f_r = \frac{1}{\pi} = 0.3183$, which is convenient for error comparisons. Second, the cosine distributions of the reflected rays allows a better comparison of the error propagation with respect to different collector patches. In our experiments we use a collector hemisphere with a resolution of 30×30 patches giving 900 outgoing directions, which would be enough to allow comparisons with a typical set of actual measurements for a single isotropic material [15].

Figure 5 presents root-mean-square (RMS) error[10] comparisons considering the three subdivisions described earlier. Although the RMS error is lower for experiments using the equal adjusted solid angle strategy, the differences decrease with an increase in the number of rays as expected.
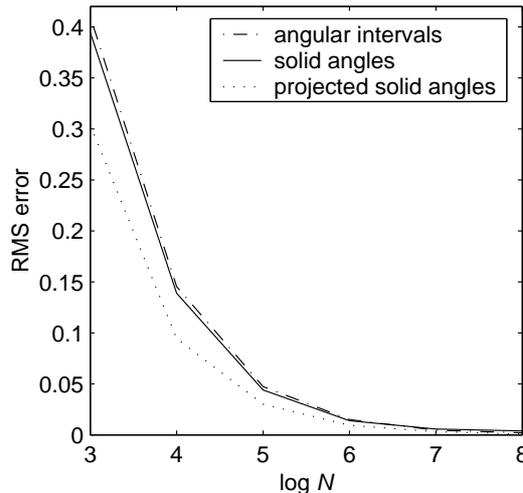
Figure 5: RMS error comparisons with respect to BRDF computation (collector hemisphere resolution: 30×30 patches) using the three subdivision techniques examined in this paper.

It is worth noting, however, that the RMS is a global measure, *i.e.*, low RMS error does not guarantee low error for individual patches. The graphs presented in Figure 6 show the BRDF values for three patches on a same plane (fixed ϕ), top, middle and bottom (grazing angle). As we can see, using the the equal adjusted solid angle strategy (Figure 6c), the BRDF values with respect to three patches converge more uniformly to the actual value than using the other techniques (Figure 6a and 6b). Also, it should be noted that the equal solid angle approach provides the worst results with respect to top patches.
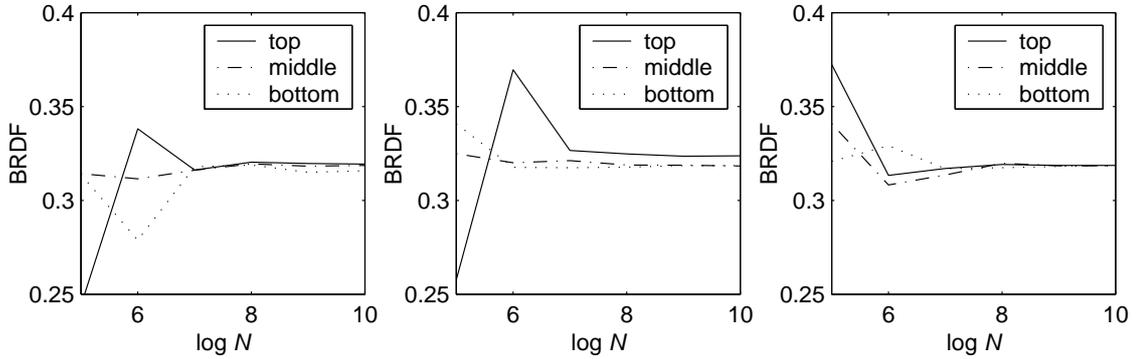
Figure 6: BRDF values for three different patches (collector hemisphere resolution 30×30 patches) using: equal angular intervals (left), equal solid angles (center) and equal projected solid angles (right).

5.2 Ray Density Bound

For virtual goniophotometric measurements aimed at rendering applications one needs solutions accurate to only 1-10%, since humans do not perceive finer variations of light. This allows us to set $\delta = 0.01$. Also, according to data provided in the measurement literature [9] the uncertainty of actual goniophotometers is around 0.5% or higher, which allows us to set $\epsilon = 0.005$. Using the presented upper bound (Equation 21), $N = m10^{5.02}$ rays are required to obtain asymptotically convergent readings is given by where m is total number of patches of the collector hemisphere. Unless otherwise stated, in the experiments presented in this section we apply the equal adjusted solid angles strategy to subdivide the collector hemisphere.

The materials used in our experiments were simulated using Monte Carlo based algorithms [21, 27]. Due to the non-deterministic nature of these simulations, one can expect fluctuations in the measurement readings when a small number of samples (N) is used [1]. These measurement readings correspond to BRDF estimates computed at individual patches, and the "spikes" observed in Figures 7- 12 for low values of N are a visual representation of these fluctuations.

We performed BRDF measurements for a diffuse material using three different resolutions for the collector hemisphere, namely 10x10, 30x30 and 100x100 patches. The diffuse material was simulated using a cosine probability distribution function [21]. Applying the presented bound (Equation 21) for the 10x10 resolution, one can expect asymptotically convergent readings using at most 10^7 rays. For the 30x30 resolution 10^8 rays are sufficient to obtain asymptotically convergent readings, while for the 100x100 resolution one would need a larger number of rays, approximately 10^9 rays according to the presented bound (Equation 21). These aspects can be visually observed in Figure 7 which presents the profiles of these BRDF measurements. These error propagation trends can also be quantitatively verified through the RMS errors presented in Table 1. Furthermore, it is worth noting that this trend is not restricted to Lambertian models as illustrated in the additional test cases presented in the remainder of this section. As mentioned earlier a Lambertian model was considered because it represents a pessimistic scenario. In other words, since all directions have equal importance, a larger N is required to obtain an asymptotically convergent BRDF estimate for each patch on the collector hemisphere.

As mentioned in Section 4, for models simulating materials with a stronger specular behavior the number of rays required to obtain asymptotically convergent results will be at least one order of magnitude smaller than the number provided by the proposed bound. We performed BRDF measurements for a specular material using three different resolutions for the collector hemisphere, namely 10x10, 30x30 and 100x100 patches. The specular material was simulated using a exponentiated cosine probability distribution function [21], considering the exponent equal to 16 and an angle of incidence of $30°$. For the 10x10 resolution, one can expect asymptotically convergent readings using at most 10^6 rays. For the 30x30 resolution 10^7 rays are sufficient to obtain asymptotically convergent readings, while for the 100x100 resolution one would need a larger number of rays, approximately 10^8 rays according to the proposed bound. These aspects can be visually observed in Figure 8 which presents the profiles of these BRDF measurements. These error propagation trends can also be quantitatively verified through the RMS errors presented in Table 2. Since we do not have an analytical value to compare with, we used as reference BRDF values obtained considering 10^{10} rays.

Since a computer model is usually less predictable than measuring physical phenomena, $i.e.$, it may work well for some input instances and fail for others, it is important to verify that the convergence of the measurements is not restricted to a single plane. Figures 9 and 10 show BRDF measurements for the same diffuse and specular materials obtained using a collector hemisphere subdivided into 30x30 patches and four different ray densities in order to illustrate the convergence of the estimates.

Most natural materials have a scattering behavior that exhibits an angular dependency on the incident angle intermediate to that expected of diffuse and specular reflector. For this reason we also considered a glossy material which was simulated using a cosine and an exponentiated

number of rays	10^5	10^6	10^7	10^8
10x10 patches	0.0102	0.0029	0.0011	0.0003
30x30 patches	0.0310	0.0095	0.0031	0.0009
100x100 patches	0.1010	0.0315	0.0099	0.0032

Table 1: RMS errors associated to BRDF measurements for a diffuse material, considering three resolutions for the collector sphere and using four ray densities.

number of rays	10^5	10^6	10^7	10^8
10x10 patches	0.0094	0.0024	0.0010	0.0002
30x30 patches	0.0305	0.0091	0.0030	0.0009
100x100 patches	0.0980	0.0326	0.0102	0.0030

Table 2: RMS errors associated to BRDF measurements for a specular material (simulated using an exponentiated cosine distribution with exponent equal to 16), considering three resolutions for the collector sphere and using four ray densities.

cosine distributions [21]. For the diffuse component we use a coefficient equal to 0.8, and for the specular component we use a coefficient equal to 0.2 and an exponent equal to 16. In order to increase our scope of observations we varied the angle of incidence, and we used a sphere subdivision scheme prone to larger variances. This scheme corresponds to the reverse of the equal adjusted solid angle subdivision, *i.e.*, the hemisphere is divided in slices along the parameter space represented by the angle ϕ, and as a consequence a larger number of smaller patches is placed on the top of the hemisphere. The results of these experiments are presented in Figure 11, and they suggested that asymptotically convergent estimates can be obtained using the presented bound (Equation 21) under these circumstances.

The materials considered above were simulated using isotropic models. Figure 12 illustrates measurements for an anisotropic material which was simulated using a Phong based distribution with exponents equal to 50 and 1000 [27], and considering an angle of incidence of $30°$. These measurements were obtained using a collector hemisphere subdivided into 30x30 patches and four different ray densities in order to illustrate the convergence of the estimates. As we can see, convergent estimates can be obtained using a number of rays one order of magnitude below the presented upper bound (Equation 21).

6 Conclusion

In this paper we examined practical issues related to the computer simulation of goniophotometers. Considering that many readings are required to obtain a comprehensive goniophotometric record for a single specimen, our discussion was focused on strategies to raise the reliability/cost ratio of readings obtained using such simulations.

From a practical point of view, selecting the "best" subdivision scheme for the collector sphere is delicate, and no single technique is superior in all cases. The relative accuracy depends on the characteristics of the specimen's BRDF. Assuming no prior knowledge about the BRDF behavior, our experiments suggest that the use of a subdivision technique based on equal adjusted solid angles may provide a more uniform convergence for the estimates than the other two techniques examined in this paper, and its implementation is equally straightforward.

Our experiments also indicate that the presented upper bound for the number of rays required to obtain asymptotically convergent estimates can be used to reduce the computational costs of the simulations. Our future efforts in this area will involve the optimization of this bound, which will require the investigation of the variance introduced by complex BRDF simulations, such as those proposed by Westin *et al.* [32], as well as bring more probability tools to bear on the problem.

Acknowledgements

References

[1] G.V.G. Baranoski, J.G. Rokne, and G. Xu. Virtual spectrophotometric measurements for biologically and physically-based rendering. *The Visual Computer*, 17(8):506–518, 2001.

[2] J. Bonner and J.E. Varner. *Plant Biochemistry*. Academic Press, New York, 1965.

[3] M.F. Cohen and D. Greenberg. The hemi-cube: A radiosity solution for complex environments. *Computer Graphics (SIGGRAPH Proceedings)*, 19(3):31–40, July 1985.

[4] D. Combes, I. Moya, J. Andlauer, S. Jacquemoud, S. Sinoquet, and C. Varlet-Grancher. Un nouveau dispositif de mesure des propriétés optiques et bidirectionnelles de surface végétales. In *8th International Symposium of Physical Measurements & Signatures in Remote Sensing*, pages 283–284, Aussois, France, 2001. CNES.

[5] B.G. Crowther. Computer modeling of integrating spheres. *Applied Optics*, 35(30):5880–5886, 1996.

[6] J. DeYoung and A. Fournier. Properties of tabulated bidirectional reflectance distribution functions. In *Proceedings of Graphics Interface*, pages 47–55, 1997.

[7] ASTM Standard E284-91C. Standard terminology of appearance. In L.B. Wolff, S.A. Shafer, and G.E. Healey, editors, *Physics-Based Vision Principles and Practice: Radiometry*, pages 146–161, Boston, 1992. Jones and Bartlett Publishers.

[8] J. Fendley. An analysis of the measuring procedure for the integrating sphere spectrophotometer. *Solar Energy*, 35(3):281–282, 1985.

[9] S.C. Foo. A gonioreflectometer for measuring the bidirectional reflectance of material for use in illumination computation. Master's thesis, Cornell University, August 1997.

[10] A.S. Glassner. *Principles of Digital Image Synthesis*. Morgan Kaufmann, San Francisco, 1995.

[11] S. Goertler, M.F. Cohen, and P. Slusallek. Radiosity and relaxation methods. *IEEE Computer Graphics and Applications*, 14(6):48–58, November 1994.

[12] J.S. Gondek, G.W. Meyer, and J.G. Newman. Wavelength dependent reflectance functions. In Andrew Glassner, editor, *Proceedings of SIGGRAPH*, pages 213–220, July 1994.

[13] Y.M. Govaerts. *A model of light scattering in three-dimensional plant canopies: a Monte Carlo ray tracing approach.* PhD thesis, Départment of Physique, Faculté des Sciences, Université Catholique de Louvain-la-Neuve, 1995.

[14] Y.M. Govaerts, S. Jacquemoud amd M. Verstraete, and S.L. Ustin. Three-dimensional radiation transfer modeling in a dycotyledon leaf. *Applied Optics*, 35(33):6585–6598, November 1996.

[15] D.P. Greenberg, J. Arvo, E. Lafortune, K.E. Torrance, J.A. Ferwerda, B. Walter, B. Trumbore, P. Shirley, S. Pattanaik, and S. Foo. A framework for realistic image synthesis. In *SIGGRAPH Proceedings, Annual Conference Series*, pages 477–494, 1997.

[16] P. Hanrahan and W. Krueger. Reflection from layered surfaces due to subsurface scattering. *Computer Graphics (SIGGRAPH Proceedings)*, pages 165–174, August 1993.

[17] R.S. Hunter and R.W. Harold. *The Measurement of Appearance*. John Wiley & Sons, New York, second edition, 1987.

[18] S. Jacquemoud and S.L. Ustin. Leaf optical properties: A state of the art. In *8th International Symposium of Physical Measurements & Signatures in Remote Sensing*, pages 223–332, Aussois, France, 2001. CNES.

[19] D.B. Judd and G. Wyszecki. *Color in Business, Science and Industry*. John Wiley & Sons, New York, third edition, 1975.

[20] K.F. Karner, H. Mayer, and M. Gervautz. An image based measurement system for anisotropic reflection. *Computer Graphics Forum (EUROGRAPHICS Proceedings)*, 15(3):119–128, August 1996.

[21] E.P. Lafortune and Y. D. Willems. Using the modified phong reflectance model for physically based rendering. Technical report, Department of Computer Science, K.U. Leuven, November 1994.

[22] P. Lalonde and A. Fournier. Generating reflected directions from brdf data. *Computer Graphics Forum (EUROGRAPHICS Proceedings)*, 16(3):293–300, September 1997.

[23] D.L. MacAdam. *Color Measurements Theme and Variations*. Springer Verlag, Berlin, 1981.

[24] S.R. Marschner. *Inverse Rendering for Computer Graphics*. PhD thesis, Cornell University, 1998.

[25] S.R. Marschner, E.O.F. Lafortune, S.H. Westin, Kenneth E. Torrance, and D.P. Greenberg. Image-based brdf measuremnt. Technical Report PCG-99-1, Program of Computer Graphics, Cornell University, January 1999.

[26] A. Nusselt. Graphische Bestimmung des Winkelverhältinesses bei der Wärmestrahlung. *Zeitschrift des Vereins Deutscher Ingenieure*, 72(20):673, 1928.

[27] M. Ashikhmin S. Premoze and P. Shirley. A microfacet-based brdf generator. In *SIGGRAPH Proceedings, Annual Conference Series*, pages 65–74, July 2000.

[28] P. Shirley. *Physically based lighting for computer graphics*. PhD thesis, Dept. of Computer Science, University of Illinois, November 1990.

[29] P. Shirley. *Realistic Ray Tracing*. AK Peters Ltd., 2001.

[30] M.J.C van Gemert, S.L. Jacques, H.J.C.M. Sterenborg, and W.M. Star. Skin optics. *IEEE Transactions on Biomedical Engineering*, 46(12):1146–1154, December 1989.

[31] G.J. Ward. Measuring and modeling anisotropic reflection. *Computer Graphics (SIGGRAPH Proceedings)*, pages 265–272, July 1992.

[32] S.H. Westin, J.R. Arvo, and K.E. Torrance. Predicting reflectance from complex surfaces. *Computer Graphics (SIGGRAPH Proceedings)*, 26(2):255–264, July 1992.

$N=10^5$ $N=10^6$ $N=10^7$ $N=10^8$
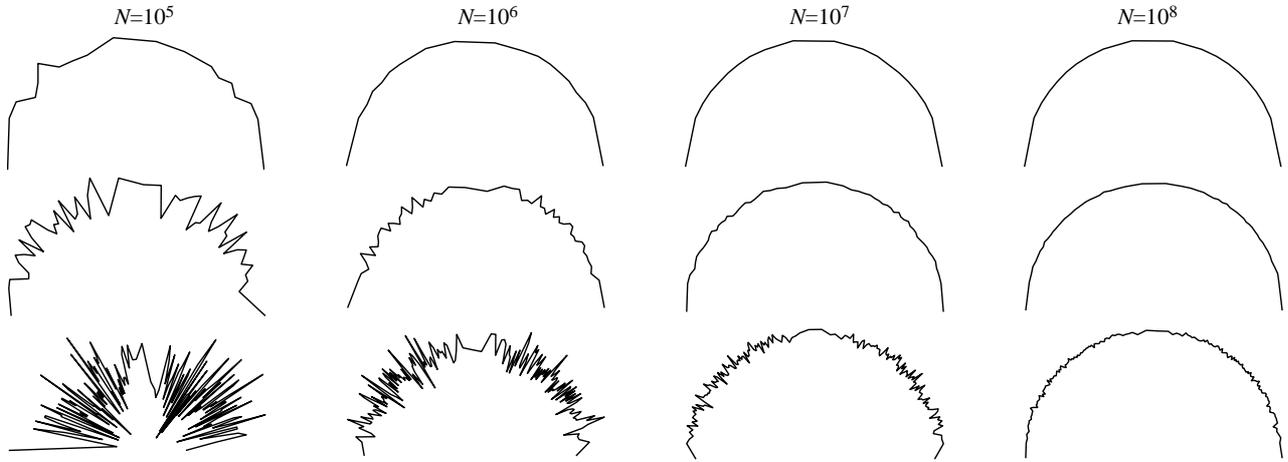
Figure 7: Profiles of BRDF measurements for a specimen whose scattering properties were simulated using a cosine distribution. Displayed measurements were taken on the plane given by the direction of the incident beam and the normal of the specimen, and using different resolution for the collector hemisphere: 10x10 patches (top), 30x30 patches (middle) and 100x100 patches (bottom).

$N=10^5$ $N=10^6$ $N=10^7$ $N=10^8$
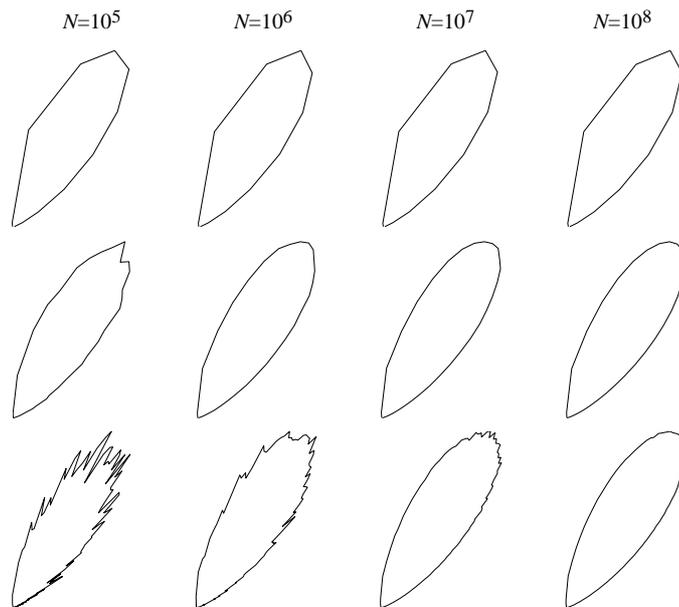
Figure 8: Profiles of BRDF measurements for a specimen whose scattering properties are simulated using a Phong based cosine lobe with exponent equal to 16. Displayed measurements were taken on the plane given by the direction of the incident beam and the normal of the specimen, and using different resolution for the collector hemisphere: 10x10 patches (top), 30x30 patches (middle) and 100x100 patches (bottom).

$N=10^5$ $N=10^6$ $N=10^7$ $N=10^8$
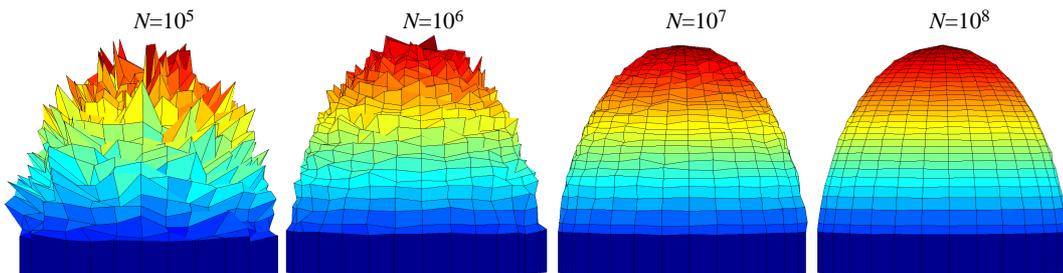
Figure 9: BRDF measurements for a specimen whose scattering properties were simulated using a cosine distribution. Displayed measurements were obtained using a collector hemisphere subdivided into 30x30 patches and four different ray densities.
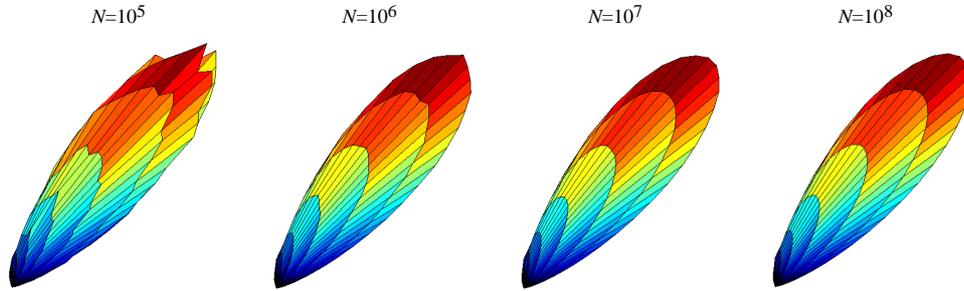
Figure 10: BRDF measurements for a specimen whose scattering properties are simulated using an exponentiated cosine distribution with an exponent equal to 16. Measurements were obtained using a collector hemisphere subdivided into 30x30 patches and four different ray densities.
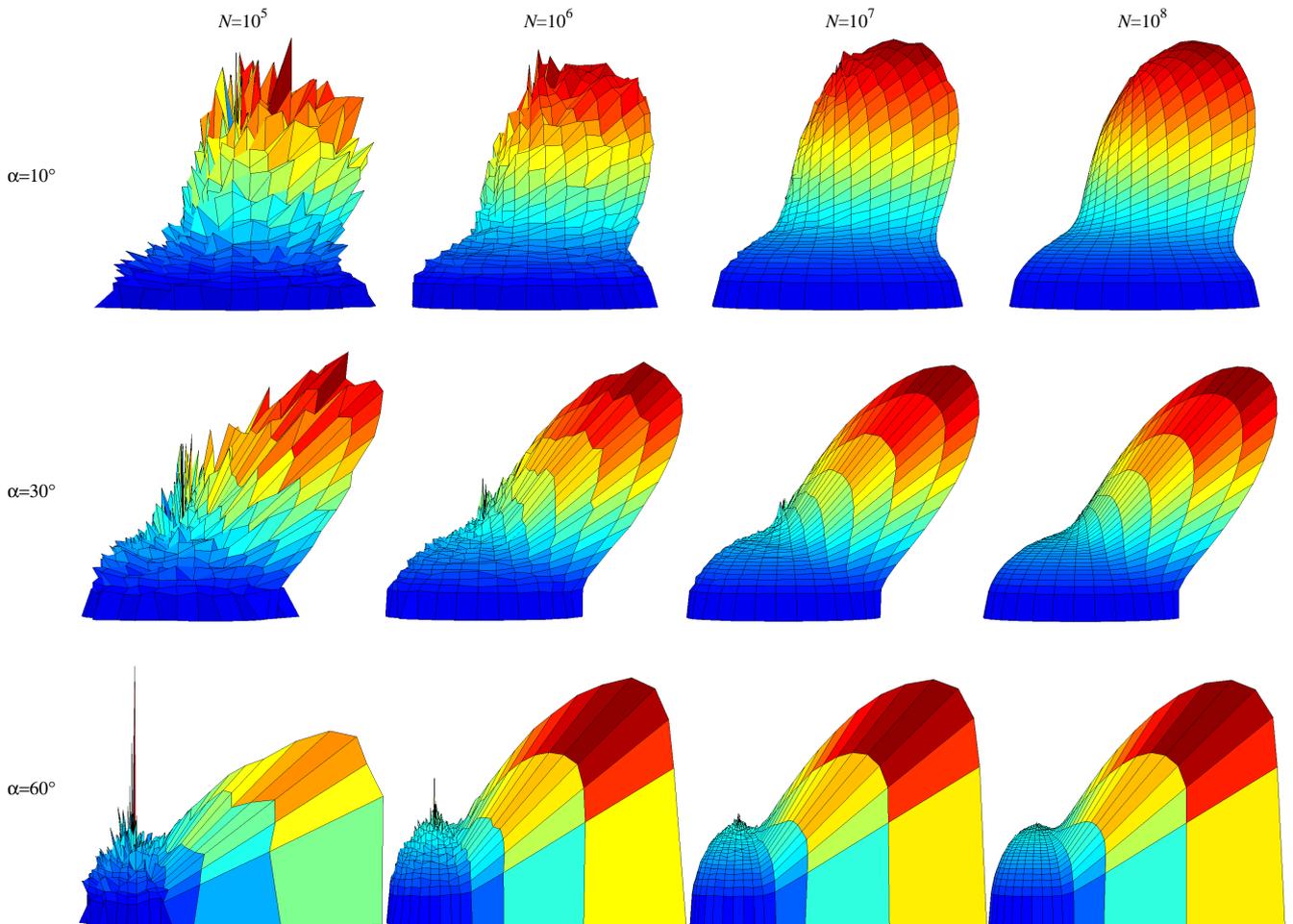
Figure 11: BRDF measurements for a glossy material obtained using a collector hemisphere subdivided into 30x30 patches, and considering four different ray densities and three angles of incidence.
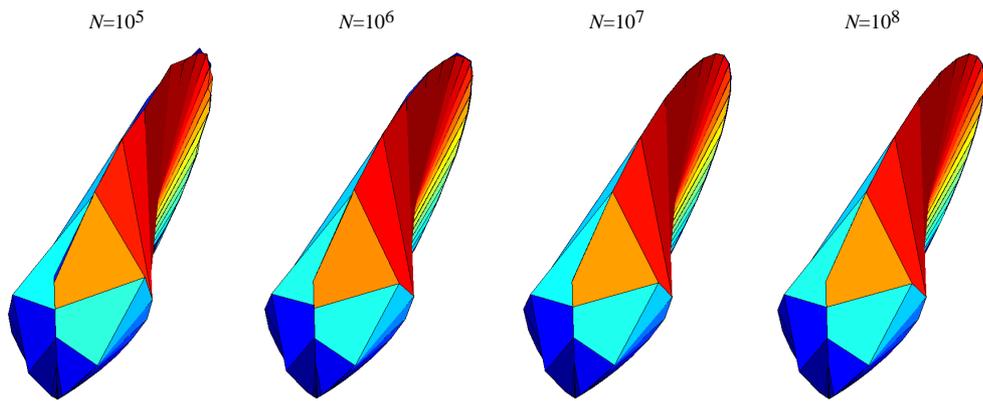
Figure 12: BRDF measurements for a specimen whose scattering properties are simulated using an anisotropic Phong based distribution with exponents equal to 50 and 1000. Measurements were obtained using a collector hemisphere subdivided into 30x30 patches and four different ray densities.